The Flavoprotein Subcomplex of Complex I (NADH:Ubiquinone Oxidoreductase) from Bovine Heart Mitochondria: Insights into the Mechanisms of NADH Oxidation and NAD^+ Reduction from Protein Film Voltammetry†

Chérise D. Barker, Torsten Reda, and Judy Hirst*

Medical Research Council Dunn Human Nutrition Unit, Wellcome Trust/MRC Building, Hills Road, Cambridge CB2 2XY, U.K.

Received September 25, 2006; Revised Manuscript Received January 18, 2007

ABSTRACT: Complex I (NADH:ubiquinone oxidoreductase) from bovine heart mitochondria contains 45 different subunits and nine redox cofactors. NADH is oxidized by a noncovalently bound flavin mononucleotide (FMN), then seven iron−sulfur clusters transfer the two electrons to quinone, and four protons are pumped across the inner mitochondrial membrane. Here, we use protein film voltammetry to investigate the mechanisms of NADH oxidation and NAD^+ reduction in the simplest catalytically active subcomplex of complex I, the flavoprotein (Fp) subcomplex. The Fp subcomplex was prepared using chromatography and contained the 51 and 24 kDa subunits, the FMN, one [4Fe-4S] cluster, and one [2Fe-2S] cluster. The reduction potential of the FMN in the enzyme's active site is lower than that of free FMN (thus, the oxidized state of the FMN is most strongly bound) and close to the reduction potential of NAD^+. Consequently, the catalytic transformation is reversible. Electrocatalytic NADH oxidation by subcomplex Fp can be explained by a model comprising substrate mass transport, the Michaelis−Menten equation, and interfacial electron transfer kinetics. The difference between the "catalytic" potential and the FMN potential suggests that the flavin is reoxidized before NAD^+ is released or that intramolecular electron transfer from the flavin to the [4Fe-4S] cluster influences the catalytic rate. NAD^+ reduction displays a marked activity maximum, below which the catalytic rate decreases sharply as the driving force increases. Two possible models reproduce the observed catalytic waveshapes: one describing an effect from reducing the proximal [2Fe-2S] cluster and the other the enhanced catalytic ability of the semiflavin state.

NADH:ubiquinone oxidoreductase (complex I), the first enzyme of the mitochondrial electron transport chain, is a highly complicated, membrane-bound enzyme comprising (in bovine mitochondria) 45 different subunits (*1*−*4*). It oxidizes NADH to NAD^+ in the mitochondrial matrix, reduces ubiquinone to ubiquinol in the inner mitochondrial membrane, and translocates protons across the membrane, contributing to the proton-motive force (*5*). Complex I is also a significant source of reactive oxygen species in the mitochondrion, and its dysfunction has been implicated in a number of neuromuscular diseases (*6*−*9*). It is an L-shaped enzyme (*10*), with one arm extending into the mitochondrial matrix and the other lying in the membrane plane. NADH is oxidized by a noncovalently bound flavin mononucleotide (FMN)[1] in the hydrophilic domain, and ubiquinone is reduced in the membrane domain. The structure of the membrane-extrinsic domain of *Thermus thermophilus* complex I shows how a "chain" of iron−sulfur (FeS) clusters [two [2Fe-2S] and six [4Fe-4S] clusters are present in bovine complex I (*3*, *11*)] extends through the protein matrix, connecting the two active sites (*12*).

In complex I, the catalytic FMN cofactor is bound by the 51 kDa subunit and connected to the protein by hydrogen bonds (*3*, *12*). The reaction between the FMN and NADH is a two-electron reaction which is very likely to be a hydride transfer reaction (*13*). The reduced flavin is reoxidized by electron transfer to the iron−sulfur clusters, presumably in two one-electron steps. However, further knowledge of both the kinetics and thermodynamics of NADH oxidation is required to understand how NADH oxidation is linked to energy transduction, conserving essentially all the free energy. Calculations based on the arrangement of the cofactors in *T. thermophilus* complex I suggest that transfer of electrons from the flavin to bound quinone is fast and not rate-limiting (*14*), but the rates of transfer of hydride from the NADH to the flavin, coupled flavin deprotonation, NADH binding, and NAD^+ dissociation are not known, and may limit the rate of delivery of electrons to the bound ubiquinone. In addition, conformational changes upon nucleotide binding have been proposed as the basis of a mechanism of energy transduction (*15*), and kinetic studies have suggested that NAD^+ is retained until the flavin is oxidized (*16*). The role of a [2Fe-2S] cluster (cluster N1a), which lies

† This research was funded by The Medical Research Council and The European Union Mitocombat program.

* To whom correspondence should be addressed: Medical Research Council Dunn Human Nutrition Unit, Wellcome Trust/MRC Building, Hills Road, Cambridge CB2 2XY, U.K. Telephone: +44 1223 252810. Fax: +44 1223 252815. E-mail: jh@mrc-dunn.cam.ac.uk.

[1] Abbreviations: DDM, *n*-dodecyl β-D-maltoside; EPR, electron paramagnetic resonance; FeS, iron−sulfur; Fp, flavoprotein; FMN, flavin mononucleotide; HAR, hexaammineruthenium(III); LB, Lineweaver−Burke; NDSB, nondetergent sulfobetaine; PGE, pyrolytic graphite edge; SHE, standard hydrogen electrode.

10.1021/bi061988y CCC: $37.00
Published on Web 02/27/2007

on the opposite side of the flavin to the clusters leading to the quinone binding site but close enough to exchange electrons with it (*12*), is unknown. It may influence the interconversion of NADH and NAD^+ at the active site and the electron distribution in partially reduced states, or help to prevent superoxide production. As there is considerable evidence to suggest that the reduced flavin is important in superoxide production by complex I (*17*), defining how the level of reduced cofactor present is determined is fundamental to understanding how superoxide production in mitochondria is controlled.

Studying the mechanism of NADH oxidation in complex I is difficult because it is fast and not rate-limiting in the NADH:ubiquinone oxidoreductase reaction. Here, we employ a simple subcomplex of complex I, the flavoprotein (Fp) subcomplex (*18*, *19*), in studying the active site and the mechanisms of NADH oxidation and NAD^+ reduction. The Fp subcomplex, as prepared here, contains the 51 and 24 kDa subunits and their associated cofactors, the FMN, one [4Fe-4S] cluster, and one [2Fe-2S] cluster, and it retains the ability to catalyze NADH oxidation. We apply protein film voltammetry, a technique in which the protein is adsorbed to the surface of an electrode and electron transfer reactions are induced, controlled, and monitored in real time using a precisely controlled electrochemical driving force (*20*−*22*), to explore the properties of the Fp subcomplex under both turnover and nonturnover conditions. In the absence of substrate, reversible reduction and oxidation of the flavin cofactor are observed. Upon addition of NADH and NAD^+, catalytic waveshapes describe the kinetics and thermodynamics of substrate interconversion. They provide new insights into the mechanism of catalysis and reveal an unusual dependence of NAD^+ reduction on thermodynamic driving force.

EXPERIMENTAL PROCEDURES

Preparation and Characterization of the Fp Subcomplex. Complex I was solubilized from bovine heart mitochondrial membranes and isolated crudely using the first Q-Sepharose chromatographic step of a published procedure (*23*). It was concentrated to 10 mg/mL using a 100 kDa polyethersulfone Vivaspin centrifugal concentrator and stored in liquid nitrogen until it was required.

All the following procedures were carried out in an anaerobic glovebox (Belle Technology, $[O_2] \sim 2$ ppm). 60 mg of complex I was diluted with buffer A [20 mM Tris-HCl, 10% ethylene glycol, and 0.1% *n*-dodecyl β-D-maltoside (DDM, Anatrace) (pH 7.5)] and incubated at 2 mg/mL with 0.5 M $NaClO_4$, 0.2% sodium cholate (Dojindo Laboratories), 0.5 mM NAD^+, and 0.5 M nondetergent sulfobetaine-201 (NDSB-201, Fluka) for 15 min at 15 °C. Cholate was included to mimic the complex I preparation used previously to prepare Fp (*24*), and the chaotrope, $NaClO_4$, was used to resolve Fp from complex I (*18*, *19*). NAD^+ helped to retain the noncovalently bound FMN in the active site (*25*), and NDSB-201 (*26*) increased the level of retention of the catalytic activity and aided chromatographic isolation. Following incubation, the mixture was concentrated by ultrafiltration (YM-30 membrane, Millipore) and diluted 3-fold with buffer A before being loaded onto a pre-equilibrated 30 mL Q-Sepharose column (GE Healthcare, 15 °C). Proteins were eluted using a shallow linear gradient of NaCl, during which the Fp subcomplex eluted at ~0.3 M. The Fp-containing fractions (typically 6 mL) were diluted 3-fold into buffer C (buffer A without DDM), loaded onto a pre-equilibrated 10 mL Q-Sepharose column at 10 °C, and eluted as before. The Fp-containing fractions were concentrated to 0.5 mL by ultrafiltration and injected onto a Superdex 200 gel filtration column (GE Healthcare, buffer C with 0.15 M NaCl, 4 °C). The Fp subcomplex eluted in a single, symmetrical peak with an apparent molecular mass of ~90 kDa. Fp-containing fractions were concentrated to 6−8 mg/mL and stored in liquid nitrogen.

Protein concentrations were determined using the Pierce bicinchoninic acid (BCA) assay, and FMN and iron concentrations were determined as described previously (*27*−*29*). SDS−PAGE, N-terminal sequence analyses, and peptide mass fingerprinting were carried out as described previously (*30*). Catalytic activity assays were carried out in 20 mM Tris-HCl (pH 7.5) at 30 °C, using NADH (typically 100 μM, Sigma) and hexaammineruthenium III (HAR, typically 1 mM, Sigma), monitored via the NADH concentration (340−380 nm; $\epsilon = 4.81\ mM^{-1}\ cm^{-1}$). EPR spectra were recorded on a Bruker EMX X-band spectrometer using an ER 4119HS cavity, maintained at low temperatures by an ESR900 continuous-flow liquid helium cryostat (Oxford Instruments); the sample temperature was measured with a calibrated Cernox resistor (Lake Shore Cryotronics Inc.).

Protein Film Voltammetry. Analogue-scan cyclic voltammetry and amperometry were carried out in an anaerobic N_2 glovebox (Belle Technology, $[O_2] < 5$ ppm) using an Autolab PGSTAT30 electrochemical analyzer (EcoChemie). Pyrolytic graphite edge (PGE) working electrodes were used with a saturated calomel reference electrode (SCE) and a platinum counter electrode. All potentials are reported relative to the standard hydrogen electrode (SHE). The all-glass electrochemical cell comprised three compartments. The central compartment was surrounded by a water jacket and thermostated using a water circulator. It housed the working electrode and contained a solution of 10 mM KCl and four buffers at 10 mM each, chosen from sodium or potassium acetate, 2-morpholinoethanesulfonic acid (MES), *N*-cyclohexyl-2-aminoethanesulfonic acid (HEPES), *N*-tris(hydroxymethyl)methyl-3-aminopropanesulfonic acid (TAPS), and 3-(cyclohexylamino)-1-propanesulfonic acid (CAPS). The pH of each solution was set before measurement and also checked, at the experimental temperature, following measurement. The reference and counter electrode compartments were separated from the working electrode compartment by a Luggin capillary side arm and a Vycor glass frit, respectively; these two compartments contained 0.1 M KCl. NADH and NAD^+ (Sigma, NAD^+ neutralized with KOH) were added from 100 mM stock solutions in Milli-Q water; when necessary, the NADH was repurified before use to remove all NAD^+ (*31*). Stationary working electrodes had an area of 0.09 cm^2, and rotating electrodes had an area of 0.0314 cm^2 and were controlled by an EG&G 636 motor. To prepare the protein film, 0.75 μL of Fp (0.7 mg/mL) was applied directly to a clean PGE surface [polished using an aqueous 1 μm alumina suspension and napped cloth (Buehler), sonicated for 30 s, rinsed, and dried] and then placed into solution in the glass cell. Reference scans were recorded in the absence of NADH, NAD^+, or subcomplex Fp. When

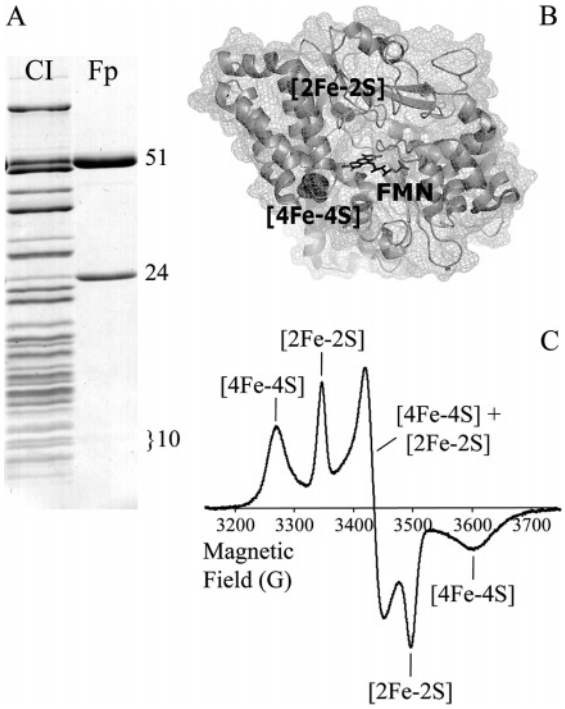

FIGURE 1: Overview of the structure and composition of the Fp subcomplex. (A) SDS−PAGE analysis of the Fp subcomplex, alongside that of complex I. The 51 and 24 kDa subunits are clearly visible, but the 10 kDa subunit is not, even though the Fp subcomplex was loaded onto the gel at a concentration significantly higher than that of complex I. (B) Structure of the NQO1 and NQO2 subunits from the hydrophilic domain of *T. thermophilus* (*12*), viewed along the channel into the NADH binding site. NQO1 is homologous to the bovine 51 kDa subunit and NQO2 to the bovine 24 kDa subunit [the levels of sequence identity are 43 and 29%, respectively (*3*)]. (C) EPR spectrum of the bovine Fp subcomplex, reduced with 5 mM sodium dithionite, recorded at 30 K to show the spectra of both the [4Fe-4S] cluster (N3) and the [2Fe-2S] cluster (N1a). g_z, g_y, and g_x = 2.05, 1.95, and 1.86, respectively, for [4Fe-4S]; g_z, g_y, and g_x = 2.01, 1.95, and 1.92, respectively, for [2Fe-2S]. Conditions: microwave frequency, 9.40 GHz; microwave power, 1 mW; modulation amplitude, 10 G; modulation frequency, 100 kHz; time constant, 20.48 ms; conversion time, 81.92 ms.

necessary, electrical noise was removed by a Fourier transformation procedure and background currents were subtracted using an in-house analysis program (courtesy of H. A. Heering, Leiden University. Leiden, The Netherlands). Modeling programs were written in C and run on Dev-C++ (www.bloodshed.net) on a desktop computer.

RESULTS

Preparation and Characterization of the Fp Subcomplex. Resolution of the Fp subcomplex from complex I, using the chaotropic anion perchlorate, was based on the procedure of Hatefi and co-workers (*18*, *19*). However, we then purified the Fp subcomplex by contemporary chromatographic methods, rather than by ammonium sulfate precipitation. The Fp subcomplex described here was both monodisperse and monomeric; it eluted in a single, symmetrical peak in the final size-exclusion chromatography step of the purification, with an apparent molecular mass of ~90 kDa. SDS−PAGE analysis (Figure 1A), in conjunction with N-terminal sequencing, confirmed that it contained the 51 and 24 kDa subunits of complex I. The 10 kDa subunit present in previous preparations (*18*, *19*) was not observed visually in SDS−PAGE analysis but could be detected by peptide mass fingerprinting of the appropriate region of the gel, indicating that low (substoichiometric) levels of the subunit were present. Figure 1B shows the structure of the NQO1 and NQO2 subunits of complex I from *T. thermophilus* (*12*), which are homologous to the 51 and 24 kDa subunits of bovine complex I, to represent the structure of the Fp subcomplex.

Preparations of the Fp subcomplex contained between 0.7 and 1.0 FMN per Fp molecule. Note that substoichiometric levels of FMN do not compromise the electrochemical experiments, as FMN-free molecules are electrochemically silent. Determination of the FMN and iron contents showed that four to five irons were present for each FMN, consistent with values reported previously (*18*, *19*). The NADH: hexaammineruthenium (HAR) oxidoreduction rate for the Fp subcomplex (using 1 mM HAR at pH 7.5 and 30 °C) varied from preparation to preparation, perhaps because of variations in the FMN content. Typically, the k_{cat} was ~500 s^{-1} (quantified using the protein concentration), and the data are characterized by an apparent K_M value of ~90 μM for NADH. These values are comparable to values from complex I, measured under equivalent conditions, suggesting [as described previously (*32*)] that the active site for NADH oxidation is not significantly disrupted by dissociation of the subcomplex.

EPR measurements on the Fp subcomplex reduced by sodium dithionite (Figure 1C) confirmed that both the [4Fe-4S] cluster bound by the 51 kDa subunit (cluster N3) and the [2Fe-2S] cluster bound by the 24 kDa subunit (cluster N1a) are present (g_z, g_y, and g_x = 2.05, 1.95, and 1.86 for [4Fe-4S] and 2.01, 1.95, and 1.92 for [2Fe-2S], respectively). The spectra are very similar to those reported previously for Fp reduced either potentiometrically or with dithionite (*33*, *34*), and the *g* values for the [2Fe-2S] cluster correlate closely to those from the overexpressed 24 kDa subunit (*35*). Although the *g* values for the [4Fe-4S] cluster match the values from previous preparations of Fp (*33*, *34*), they differ slightly from those of the equivalent cluster in complex I [g_z, g_y, and g_x = 2.04, 1.93, and 1.86, respectively (*11*)]. The structure of the hydrophilic domain of complex I from *T. thermophilus* (*12*) shows that the [4Fe-4S] cluster is located close to the interface between the 51 and 75 kDa subunits, so a change in its environment, which may affect its *g* values and relaxation properties, is expected upon dissociation of the subcomplex.

Oxidation and Reduction of the FMN in the Active Site of the Fp Subcomplex. Figure 2A compares a voltammogram from the Fp subcomplex adsorbed on a stationary pyrolytic graphite edge (PGE) electrode at 4 °C to the control (background) voltammogram recorded without the enzyme. The inset shows the two pairs of signals which are observed (marked 1 and 2) following subtraction of the background current, and compares them with theoretical waveshapes, calculated using the Nernst equation for a two-electron cofactor such as a flavin (*36*). Peak-to-peak separations are small (20−25 mV), confirming that the electroactive species are adsorbed on the electrode surface, and although the pairs of peaks are not completely symmetrical (probably because of inaccuracies in subtracting the background from such small signals), they can be reproduced accurately by two independent pairs of Nernstian waveshapes. The average

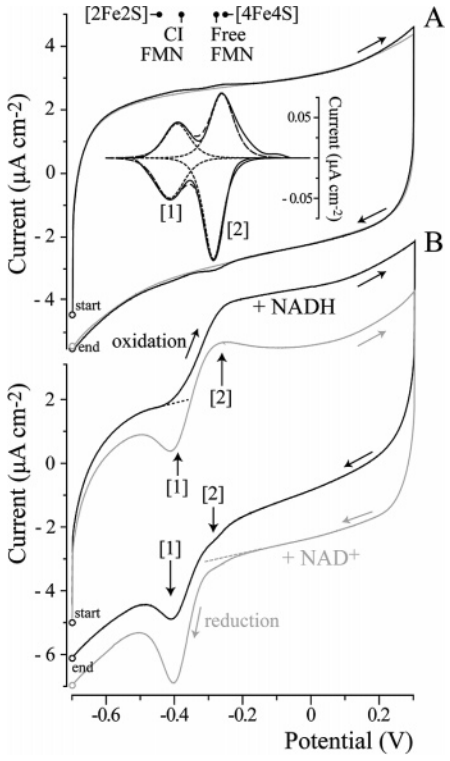

FIGURE 2: Relationships in potential between the noncatalytic signals, NADH oxidation and NAD$^+$ reduction. (A) Voltammetry of the Fp subcomplex adsorbed on the electrode surface (black), compared to the control (background) experiment in the absence of adsorbed protein (gray). Two peaks from the Fp sample are present in both the oxidative (positive) and reductive (negative) scan directions. The inset shows background-subtracted signals compared to calculated Nernstian waveshapes (intensities adjusted to match the data). The two couples have midpoint potentials of −0.401 V [1] (−0.412 and −0.390 V) and −0.262 V [2] (−0.283 and −0.241 V). The reduction potential of free FMN, measured in a separate experiment, and the potentials expected for the three redox centers in Fp are marked at the top of the figure (●) for comparison [FMN and the [4Fe-4S] cluster measured in complex I by EPR (*37*) and the [2Fe-2S] cluster measured voltammetrically in the overexpressed subunit (*35*)]. (B) Electrocatalytic voltammograms displaying the oxidation of NADH and the reduction of NAD$^+$, recorded in 0.1 mM NADH (black) and 0.1 mM NAD$^+$ (gray), under the same conditions as in panel A (arrows indicate the positions of the peaks of [1] and [2]). In the black trace (starting from −0.7 V), a sigmoidal wave is observed close to couple [1] from NADH oxidation, the current is maintained by diffusion of NADH at higher potentials, and then a peak-shaped feature is observed in the reductive scan as NADH oxidation stops and NAD$^+$, produced during the scan, is re-reduced. In the gray trace (starting from −0.7 V), NAD$^+$ is oxidized from the start of the scan, with the catalytic current displaying an unusual "minimum peak" close to couple [1]. NAD$^+$ reduction stops at a higher potential, and a "maximum peak" occurs as the generated NADH is reoxidized. On the return scan, a sharp peak is observed as NAD$^+$ reduction is reinitiated. Conditions: pH 8.05, 4 °C, subcomplex Fp adsorbed on a stationary PGE electrode, scan rate of 25 mV/s.

potentials for the two pairs of peaks are −0.401 [1] and −0.262 V [2], and the known potentials of the three redox centers in the Fp subcomplex and of free FMN are indicated at the top of the figure for comparison. The potential of couple [1] agrees well with that reported for the FMN in the active site of complex I (*37*), and its peak half-height widths are ∼85 mV, consistent with couple [1] comprising two one-electron redox couples with potentials which are close together, or a cooperative two-electron couple for which the peaks are broadened slightly due to inhomogeneous adsorption on the electrode surface (*22*, *38*). The potential of couple [2] agrees closely with that recorded for free FMN in separate experiments. Two further pairs of signals are expected from the Fp subcomplex, from the [4Fe-4S] and [2Fe-2S] clusters (potentials marked in Figure 2A), but they have not been observed. Their peak areas should be only half that of couple [1], so they are probably difficult to resolve from the background current and/or obscured by the two larger signals.

Figure 2B shows how the reversible voltammetry of Figure 2A is transformed upon the addition of NADH or NAD$^+$. Importantly, no currents from NADH oxidation or NAD$^+$ reduction were observed in the absence of the Fp subcomplex or in control experiments in which FMN alone was adsorbed on the electrode surface, confirming that NADH oxidation and NAD$^+$ reduction result only from the adsorbed enzyme. NADH oxidation is observed at potentials above −0.4 V, and the catalytic current displays a sigmoidal potential dependence, as displayed by the oxidative scan recorded in the presence of NADH. NAD$^+$ reduction is observed below −0.3 V and exhibits an unusual waveform. Importantly, the sigmoidal components from both catalytic processes exhibit similar "half-wave" potentials (approximately −0.35 V) which are close to the reduction potential of NAD$^+$, showing that the catalytic conversion is reversible (*39*). Note that in these experiments the electrode was stationary (not rotating) so that the NAD$^+$ formed from NADH oxidation remains close to the electrode to be re-reduced during the return scan (and vice versa). The lower temperature (4 °C) was chosen to facilitate the observation of both noncatalytic and catalytic signals on the same scale. Close inspection of Figure 2B reveals that the catalytic features correspond closely in potential to couple [1], confirming that couple [1] results from FMN in the active site of the Fp subcomplex, present in a catalytically active state on the electrode surface. The peaks from couple [2] are retained in the presence of substrate (most evident in the reductive scan direction), indicating that couple [2] does not participate in catalysis and consistent with the suggestion that it results from FMN which has dissociated from the enzyme.

Experiments over a range of pH values showed that the potential of couple [1], the active site FMN, matches closely to values reported previously for the FMN in complex I, measured by EPR using redox mediators (*37*) (Figure 3). The pH variation can be explained using the appropriate thermodynamic scheme (Figure 3), with the switch from two electrons and two protons at low pH (FMN/FMNH$_2$) to two electrons and one proton at high pH (FMN/FMNH$^-$) described by a pK_{red2} value of 7.8, close to that reported from EPR (7.1) (*37*). To confirm that couple [2] corresponds to free FMN, separate experiments were carried out to measure the reduction potential for FMN itself by adsorbing a small aliquot of a commercially supplied sample to the electrode surface. Figure 3 shows that the reduction potential from the known FMN sample corresponds closely to that of couple [2] over all pH values. These data can be modeled using a pK_{red2} of 8.8, a value higher than that reported previously for free FMN in solution (6.7−7.8) (*40*), perhaps because the flavin is adsorbed on the PGE surface.

Oxidation of NADH Catalyzed by Subcomplex Fp on the Electrode Surface. To learn about catalytic processes in the

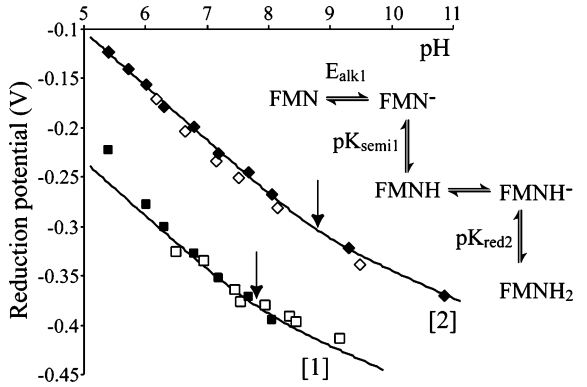

FIGURE 3: pH dependence of the potentials of the noncatalytic signals from the Fp subcomplex. Data points recorded using the Fp subcomplex are from couples [1] (■) and [2] (◆), assigned to active site and free FMN. Potentials from free FMN adsorbed at a similar concentration on the electrode surface in separate experiments (◇) and for the FMN in complex I determined using EPR (□) (*37*) are also shown. The data are fit using the scheme shown with a pK_{red2} of 7.8 (arrowed, FMN in the Fp subcomplex) and a pK_{red2} of 8.8 (arrowed, free FMN). Conditions: scan rate of 25 mV/s, 4 °C, stationary electrode.

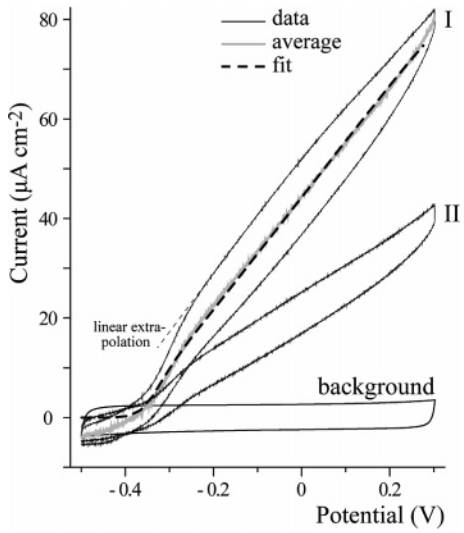

FIGURE 4: Catalytic NADH oxidation by the Fp subcomplex adsorbed on a PGE electrode. Two consecutive cycles, initiated from −0.5 V, are shown. For the first cycle (I), the forward and reverse scans were averaged, and then the reference was subtracted to obtain the final voltammogram (gray line). The model (dashed line; for parameters see Table 1 and Table S1) fits the experimental data well. The shape of the voltammogram is retained in cycle II, but the catalytic activity is decreased significantly (∼50%). Conditions: pH 7.9, 4.8 mM NADH, electrode rotation rate of 1600 rpm, potential scan rate of 25 mV/s, 30 °C.

enzyme, mass transport and interfacial electron transfer should ideally be fast (not rate-limiting) and well-characterized. Therefore, catalysis was studied using a rotating electrode to supply substrate to the electrode surface (and remove product from it) at a rapid, defined rate. Experiments were carried out at 30 °C to increase the rate of turnover (and hence the signal-to-noise ratio). Under these conditions, catalytic waveshapes for the oxidation of NADH by subcomplex Fp are sigmoidal at low overpotentials but become linear at higher potentials (see Figure 4). These semi-sigmoidal waveshapes are unusual from an electrochemical viewpoint, but similar waveshapes have been observed previously from a number of enzymes, including NiFe

Scheme 1: Model Applied To Interpret the Voltammetry of NADH Oxidation by the Fp Subcomplex[a]

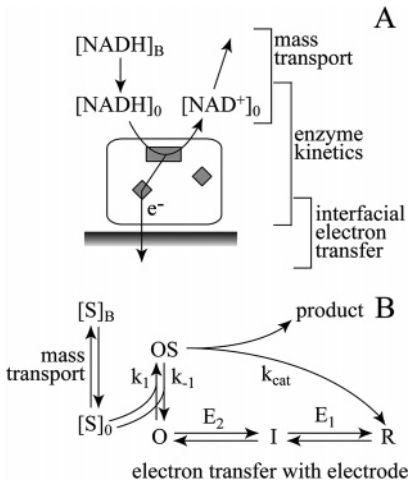

[a] O, I, and R are the oxidized, intermediate, and reduced states of the active site FMN, respectively. OS is the enzyme−substrate complex. $[S]_B$ and $[S]_0$ are the concentrations of substrate in bulk solution and at the electrode surface, respectively. $K_M = (k_{cat} + k_{-1})/k_1$. $E_{AV} = (E_1 + E_2)/2$. $\Delta E = E_2 - E_1$.

hydrogenase (*41*), arsenite oxidase (*42*), and subcomplex Iλ from bovine complex I (*43*). One possible explanation is that different orientations of the enzyme molecules on the surface have different interfacial electron transfer rates, with the observed catalytic wave being formed by the superposition of the catalytic waves from each orientation (*41*). NADH oxidation by the Fp subcomplex also depends on the NADH concentration at the electrode surface, determined by its rate of consumption by the enzyme, the concentration in the bulk solution, and mass transport to the surface. Therefore, the model applied previously to describe electrocatalytic NADH oxidation by subcomplex Iλ from bovine complex I (Scheme 1) (*43*), comprising substrate mass transport and concentration, enzyme kinetics according to the Michaelis−Menten equation, and interfacial electron transfer, is an appropriate extant model. Derivation and application of the equation used to simulate voltammograms according to Scheme 1 have been described in detail previously (*43*); it is stated in the Supporting Information as eq S1.

Figure 4 shows a typical set of electrocatalytic voltammograms for NADH oxidation by subcomplex Fp, modeled according to Scheme 1 (using eq S1), and demonstrating that the catalytic waveshape for NADH oxidation is reproduced accurately. Table S1 of the Supporting Information lists the electrochemical parameters which were used to model the experimental data, and Table 1 lists the parameters which pertain to the enzyme. However, the data shown in Figure 4 are not sufficient to define unique values for every parameter of interest, and the instability of the current (due to degradation or desorption of the enzyme) hinders the quantitative comparison of different protein films. Thus, Figure 5 shows an example of an experiment aimed at determining the dependence of the catalytic current on NADH concentration. Figure 5 shows the results from three different protein films. The potential was held at 0 V, with the electrode rotating, and the current monitored over time and upon the addition of aliquots of NADH. The step increases in current were measured, and the corresponding

Table 1: Enzyme-Specific Parameters Used To Describe Electrocatalytic NADH Oxidation by the Fp Subcomplex

parameter	definition	value		
		pH 6.81	pH 7.93	pH 9.31
Γ_{total} (mol/cm^2)	electrode coverage	7.63×10^{-13} average value estimated in the absence of substrate (e.g., Figure 2)		
ΔE (V)	difference between the two flavin potentials ($E_2 - E_1$)	−0.08 V, from EPR (*37*)		
E_{AV} (V)	average of two flavin potentials (catalytic value, e.g., Figure 4)	−0.285	−0.325	−0.355
E_{AV} (V)	average of two flavin potentials (noncatalytic value, Figure 3)	−0.330	−0.385	−0.425
k_{cat}^{app} (s^{-1})	estimated k_{cat} from LB analysis (e.g., Figure 6A)	400	610	400
k_{cat} (s^{-1})	rate constant for substrate transformation (complete analysis, Figures 4 and 6)	>900	>1300	>800
K_M (μM)	Michaelis−Menten constant estimated from LB analysis (e.g., Figure 6A)	29	212	280

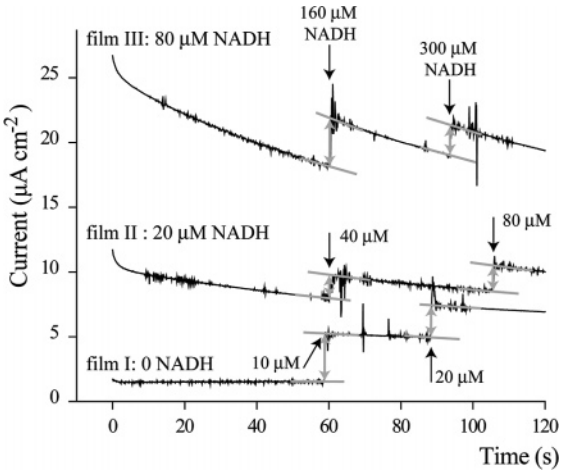

FIGURE 5: Determination of the dependence of the rate of electrocatalytic NADH oxidation on NADH concentration. Three different protein films were used, with initial NADH concentrations of 0, 20, and 80 μM. In each case, NADH aliquots were injected after 60 and 90 s, and the resulting increases in current were determined (gray arrows). Conditions: pH 6.8, electrode rotation rate of 1600 rpm, 30 °C, +0.007 V (=E_{AV} + 0.3 V).

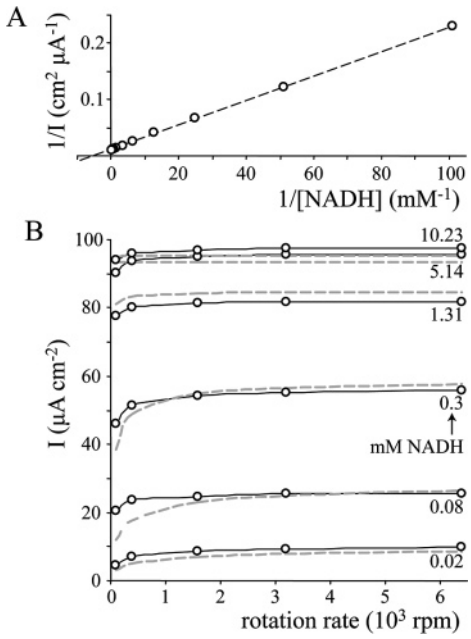

FIGURE 6: Modeling of the data from NADH concentration−rotation rate step experiments on catalytic NADH oxidation by the Fp subcomplex. (A) Catalytic current at 0.007 V (=E_{AV} + 0.3 V) as a function of the NADH concentration (1600 rpm) in a Lineweaver−Burke (LB) plot, together with the linear fit: K_M = 212 μM and I_{max} = 90.1 μA/cm^2 (thus, k_{cat}^{app} = 612 s^{-1}, assuming a surface coverage of 7.63×10^{-13} mol/cm^2). (B) Catalytic current as a function of electrode rotation rate, at various NADH concentrations. The best fit from eq 1 and the parameters in Tables 1 and S1 is shown as dashed lines. Conditions: pH 7.93, 30 °C.

percentage increases were calculated. By considering the results from a number of experiments, in which the NADH concentration or rotation rate was varied, a consistent picture of how the current depends on both variables was constructed. Experiments such as that in Figure 5 were used to construct Lineweaver−Burke (LB) plots, as shown in Figure 6A, and thus to estimate apparent K_M and k_{cat} values (see Table 1). A complete "two-dimensional" plot, along with the fit generated using eq S1, and the parameters in Tables 1 and S1, is shown in Figure 6B.

Figure 6A provides values of 0.21 mM for K_M and 610 s^{-1} for k_{cat}, at pH 7.9. Equivalent analyses at pH 6.8 and 9.3 are reported in Table 1. For comparison, solution measurements using 1 mM HAR at pH 7.5 and 30 °C typically yielded a K_M of ~90 μM and a k_{cat} of ~500 s^{-1}. Note that the voltammetric k_{cat} comprises only NADH oxidation, but in the solution assays k_{cat} includes reoxidation of the enzyme by HAR. In addition, because Lineweaver−Burke plots could not be constructed at infinite overpotentials or infinite rotation rates, the k_{cat} value from Figure 6A is an underestimate. Subsequently, analysis of the complete data set (Figure 6B), in combination with observed catalytic waveshapes (as shown in Figure 4), using eq S1, showed that the true k_{cat} value is greater than 1300 s^{-1} at pH 7.9 (see Table 1). A unique value for k_{cat} cannot be defined because modeled voltammograms depend on k_{cat} in combination with electrochemical parameters that are not easily quantified (see the Supporting Information).

Two conclusions may be drawn from the data and simulations presented in Figures 4−6. First, electrocatalytic NADH oxidation conforms to Scheme 1. Although the complete electrochemical model is complicated (requiring consideration of a distribution of interfacial electron transfer rate constants), enzyme turnover can be described adequately by the Michaelis−Menten equation, using the same k_{cat} and K_M values over the entire potential range. Second, E_{AV}

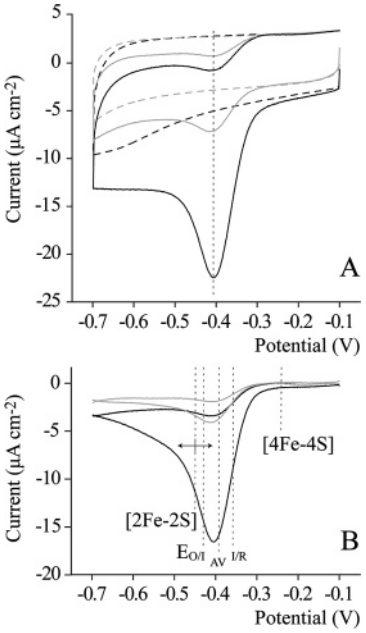

FIGURE 7: Catalytic reduction of NAD^+ by the Fp subcomplex adsorbed on a PGE electrode. (A) Two consecutive scans (black and gray), initiated from −0.1 V, are shown together with their reference scans (dashed line). (B) Background-corrected data derived from panel A, with potentials of the FeS clusters and the FMN (O, oxidized; I, intermediate oxidation state; R, reduced) (*35*, *37*). Conditions: pH 8.3, 100 μM NAD^+, electrode rotation rate of 1600 rpm, potential scan rate of 25 mV/s, 30 °C.

determined under turnover conditions (read from the voltammetric waveshape as the "half-height" of the sigmoidally shaped portion of the voltammogram, or determined by fitting voltammetric waveshapes as shown in Figure 4) is not equal to E_{AV} determined in the absence of substrate (see Table 1). Specifically, E_{AV} is 45−70 mV higher when measured during catalysis. Possible explanations for this behavior, relevant to the mechanism of NADH oxidation, are discussed below.

Reduction of NAD^+ Catalyzed by Subcomplex Fp on the Electrode Surface. Figure 7 displays the catalytic reduction of NAD^+ by the Fp subcomplex adsorbed on a PGE electrode surface. The waveshape differs significantly from that of NADH oxidation − following the expected increase in rate as the potential is decreased, the catalytic current drops sharply. The apparent "switching" potential (the "peak" potential; see Figure 7) is −0.41 V (pH 8.3), close to the two-electron potential of the FMN (−0.4 V at pH 8.3; see Figure 3) and to the potential of the [2Fe-2S] cluster in the 24 kDa subunit (−0.415 to −0.485 V, depending on the ionic strength) (*35*). Although the catalytic current decreases continuously throughout the experiment, the negative peak is present in both scan directions, showing that the switch is reversible (the enzyme "switches off" at low potentials and "back on" at higher potentials). Voltammograms recorded at different pH values (6.5−9.5), under the same conditions, showed that the switching peak potential depends on pH by approximately 60 mV per decade, indicating that it results from a redox couple with one proton to one electron stoichiometry. However, the [2Fe-2S] cluster (*35*), the two-electron FMN couple (see Figure 3), and both one-electron FMN transitions (*37*) may exhibit similar pH dependencies. Finally, experiments conducted at higher NAD^+ concentrations showed a less pronounced peak, suggesting that the

Scheme 2: Models Applied To Interpret the Voltammetry of NAD^+ Reduction by the Fp Subcomplex[a]

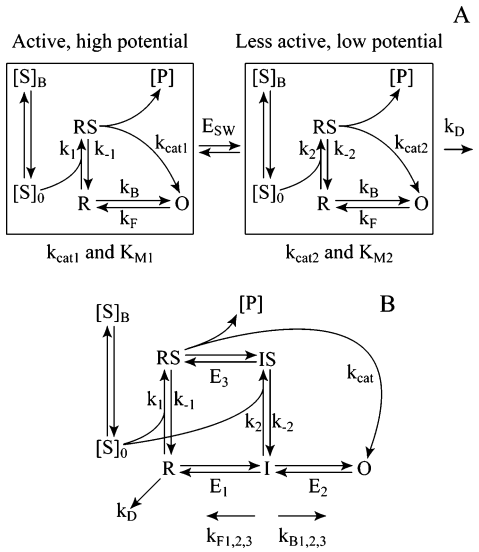

[a] O, I, and R are the oxidized, intermediate, and reduced states of the active site, respectively. IS and RS are enzyme−substrate complexes. $[S]_B$ and $[S]_0$ are the concentrations of substrate in bulk solution and at the electrode surface, respectively. E_{SW} denotes conversion between two different forms of the enzyme according to the potential, and k_D denotes irreversible conversion to an inactive state.

switch is between two different forms of the enzyme with different substrate affinities. We propose two models which predict waveshapes consistent with the observed waveshapes.

Model 1 (Scheme 2A) includes two different enzyme forms with different K_M and k_{cat} values, interconverted by a separate redox couple with a reduction potential E_{SW}. Here, the switch is proposed to be the [2Fe-2S] cluster so that E_{SW} is a one-electron transition, and interconversion of the two enzyme forms is fast and set by the Nernst equation. The equations used to implement model 1 mathematically are derived in the Supporting Information, by balancing mass transport against enzyme turnover (*44*). For simplicity, only one value of k_0, the interfacial electron transfer rate constant, is considered (the effects of different enzyme orientations on the electrode surface are not included). Model 1 also includes the first-order loss of the less active enzyme, due to either denaturation or desorption, as the overall catalytic current decays significantly during each experiment. Note that this process is much slower than catalytic turnover and so is considered outside of the steady-state assumption held, for catalysis, at each point on the potential scale. Figure 8A shows an example of a voltammogram simulated using model 1, corresponding to the data shown in Figure 7. The parameters used are reported in the legend of Figure 8A but are not intended to define a unique set of values. Values of E_{AV} and E_{SW} are consistent with those expected for the FMN and the [2Fe-2S] cluster, and the K_M value for the less active form is higher than that of the active form. The two k_{cat} values are similar.

Model 2 (Scheme 2B) incorporates a second pathway for reaction via binding of the substrate to the intermediate reduction state of the FMN. As for model 1, for simplicity model 2 considers only one value for k_0, and the denaturation or desorption of species R, the species with an unoccupied, reduced active site, is included. Figure 8B shows that

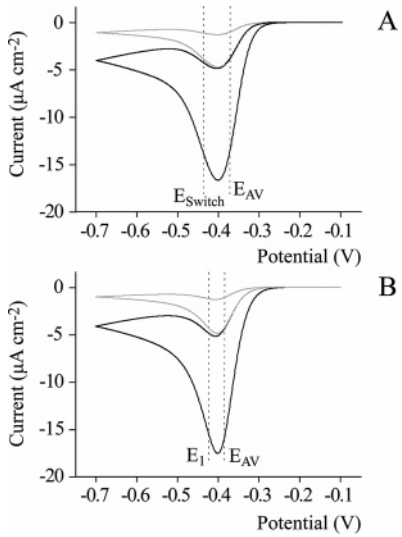

FIGURE 8: Modeled catalytic waveshapes for the reduction of NAD$^+$ by the Fp subcomplex. (A) Two consecutive scans corresponding to the data shown in Figure 7B, calculated using model 1 (Scheme 2A). The following parameters were used: $E_{AV} = -0.372$ V ($n = 1.6$), $k_{cat1} = 305$ s^{-1}, $K_{M1} = 80$ μM, $E_{SW} = -0.438$ V, $k_{cat2} = 215$ s^{-1}, $K_{M2} = 285$ μM, and $k_D = 0.064$ s^{-1}. (B) Two consecutive scans corresponding to the data shown in Figure 7B, calculated using model 2 (Scheme 2B). The following parameters were used: $E_1 = -0.344$ V, $E_2 = -0.424$ V ($E_{AV} = -0.384$ V), $k_1 = 605$ s^{-1}, $K_{d(R)} = 50$ μM, $k_2 = 25\,700$ s^{-1}, $K_{d(I)} = 50$ μM, $k_{cat} = 30\,000$ s^{-1}, and $k_D = 0.06$ s^{-1}.

simulations using model 2 may also give rise to catalytic waveshapes which are consistent with the observed waveshapes. However, the very low values of Γ_I which are achieved, even at E_{AV}, mean that $k_2 \gg k_1$ and also that k_{cat} must be very large, casting doubt on the validity of this model.

DISCUSSION

The relatively small size and simplicity of the Fp subcomplex have allowed the two-electron potential of the active site FMN in complex I or one of its subcomplexes to be measured, for the first time, under conditions in which the enzyme is catalytically active. The reduction potential is pH-dependent, so it describes the FMN/FMNH$_2$ conversion when pH < pK_{red2}, and the FMN/FMNH$^-$ conversion when pH > pK_{red2}. The values determined here correspond closely to those determined previously by EPR (*37*) (see Figure 3), although the best-fit value for pK_{red2} (7.8) differs slightly from that reported previously (7.1). The fact that the reduction potential of the active site FMN is significantly lower than that of free FMN shows that the oxidized state is significantly more strongly bound to the enzyme than the reduced state. Estimated from Figure 3, the dissociation constant is $\sim 6 \times 10^4$ times smaller for FMNH$_2$ than for FMN (pH 6) and $\sim 7 \times 10^3$ times smaller for FMNH$^-$ than for FMN (pH 10). The structure of the hydrophilic domain of *T. thermophilus* complex I shows two hydrogen bonding interactions with the oxidized isoalloxazine ring system, and a conserved glutamate residue is poised above the *re* face (but outside of hydrogen bonding distance) (*12*). How the interactions between the flavin and the protein respond to a change in the flavin's oxidation state is not yet clear, though we note that a conformational change upon the reduction of complex I by NADH has been proposed (*15*). The more negative reduction potential of the bound FMN may be required for more efficient energy conservation, as the FMN potential is brought down to match that of NADH [−0.368 V (FMN, Figure 3) vs −0.335 V (NADH) (*39*) at pH 7.5]. Finally, signals from the two iron−sulfur clusters in the Fp subcomplex have not been observed voltammetrically, probably because they are both smaller and broader than that of the FMN (*22*), which is already difficult to resolve from the electrode background capacitance.

NADH oxidation by the Fp subcomplex can be modeled by Scheme 1, using parameters which are consistent with those from conventional catalytic activity assays (see Tables 1 and S1). There are no discontinuities in the potential−current relationship, indicating that a single mechanism operates over the whole potential range, but the voltammograms display an extended increase in current with potential, most likely because k_{cat} is high and interfacial electron transfer is unable to maintain the active site FMN under Nernstian equilibrium (*41*, *43*). Importantly, the potential of the active site deduced from modeling the catalytic voltammetry does not accurately match the potential measured in the absence of substrate (see Table 1). We suggest the following two explanations.

(i) The Fp subcomplex does not obey Michaelis−Menten kinetics; in particular, substrate binds to more than one oxidation state of the active site, or product dissociation is rate-limiting and so product is retained during active site reoxidation. The presence of a nucleotide in the active site would affect its reduction potential and shift the catalytic wave. In the simplest situation, the FMN potential is expected to shift positively when NAD$^+$ is bound and negatively when NADH is bound, indicating that the NAD$^+$-bound state is being detected here. Interestingly, an ordered mechanism has been proposed for the NADH:HAR oxidoreductase reaction in complex I (NAD$^+$ is retained in the active site until the flavin is oxidized) (*16*). No consensus has been reached on the dissociation constants for binding of NADH and NAD$^+$ to complex I (see, for example, refs *45* and *46*), but voltammetry has been used to define the expected negative shift in potential of the FAD cofactor in fumarate reductase from *Escherichia coli* upon succinate binding (*47*).

(ii) The apparent active site potential during turnover is influenced by the potential of the [4Fe-4S] cluster (N3) in the 51 kDa subunit, a possible electron relay site between the electrode and the FMN, which has a more positive reduction potential than the FMN [ca. −0.25 V (*11*)]. A number of reports have described previously how the apparent active site potential during catalysis reflects that of a relay site (rather than that of the active site) (*48*−*50*), and it has been proposed that apparent catalytic potentials can be used to deduce information about the identity of the rate-limiting step (*20*, *51*). Recently, mathematical modeling has confirmed that rate-limiting intramolecular electron transfer through a single relay site may indeed result in an apparent active site potential that reflects the potential of the relay site (*52*). Thus, a shift in the apparent active site potential toward the potential of the relay, as observed here, suggests that intramolecular electron transfer and the catalytic transformation occur on comparable time scales. In the Fp subcomplex, intramolecular electron transfer from the flavin to the [4Fe-4S] cluster occurs twice during a single turnover, and it is coupled to deprotonation of the reduced flavin

species. Although uncoupled electron transfer between the flavin and the cluster is predicted, from the distance between them, to occur on a nanosecond time scale (*14*), it is possible that coupled deprotonation slows the intramolecular electron transfer event (*53*) and that the influence of this step on the rate of NADH oxidation by complex I should be considered.

The characteristics of NAD^+ reduction by the Fp subcomplex are unusual and more complex than those of NADH oxidation. However, similar behavior has been observed previously for a number of different enzymes (*54*). In succinate dehydrogenase from bovine mitochondria, fumarate reduction has a sharp activity maximum at a potential close to that of the active site flavin (*51*, *55*). It was suggested that, when the reduced state of the flavin persists during steady-state turnover, a conformational change produces a less active form of the enzyme. A conformational change in the flavin has previously been characterized and suggested to control the reactivity of *p*-hydroxybenzoate hydroxylase (*56*). In cytochrome *c* nitrite reductase, maximum nitrite reduction occurs at the reduction potentials of two heme centers which are part of the electron relay to the active site (*57*−*59*), and in fumarate reductase from *E. coli*, the oxidation state of a low-potential [4Fe-4S] cluster in the electron relay also has significant effects on catalysis (*60*). In the molybdoenzymes DMSO reductase (*61*) and nitrate reductase (*62*−*65*), the activity maximum at intermediate potential has been attributed to the substrate binding properties of the Mo(V) oxidation state. Notably, for DMSO reductase, the activity maxima for reductive and oxidative catalysis coincide (*61*).

For the Fp subcomplex, we have identified two possible mechanisms. Although the potential of the switch matches the two-electron potential of the FMN, suggesting an additional possibility, the activity maximum is at the same potential in both scan directions. This observation indicates that the switch is controlled thermodynamically, not kinetically; however, a thermodynamically controlled decrease in the capability of the fully reduced flavin to oxidize NAD^+ only decreases the intensity of the catalytic voltammogram, and does not alter its shape. Model 1 (Scheme 2A and Figure 8A) proposes that the reduction of the [2Fe-2S] cluster produces an enzyme state with lower catalytic activity. The [2Fe-2S] cluster in the 24 kDa subunit is approximately 14 Å from the FMN, yet it does not form part of the chain of cofactors between the two active sites in complex I (see Figure 1B) (*12*). It is possible that increased negative charge on the cluster alters the electrostatic environment at the binding site and decreases the affinity or rate of NAD^+ binding or that redistribution of electrons between the flavin and the cluster is disrupted during flavin reoxidation. Model 2 (Scheme 2B and Figure 8B) proposes that the semiflavin state is more reactive than the fully reduced flavin, because it binds substrate either more tightly or more rapidly. However, if the population of the semiflavin state is determined by the two potentials found previously by EPR (*37*), then its population is always so low that the rate of reaction via the semiflavin pathway must be comparatively very high, and current knowledge suggests no explanation for such a large difference in rate. Note that models 1 and 2 have been optimized by considering that enzyme denaturation or desorption occurs most rapidly at lower potential (in model 1 the less active state is unstable, and in model 2 denaturation occurs when the flavin is reduced and no nucleotide is bound). There is no direct evidence to support these proposals, but it is known that the flavin dissociates more readily when it is reduced (*25*). Finally, irrespective of the molecular mechanism of the switching process, under a high membrane potential and with a reduced quinone pool it may be possible to achieve the low potentials required to begin to switch complex I off. Consequently, as the thermodynamic driving force for NAD^+ reduction [in reverse electron transport (*66*)] increases, its rate will actually decrease, hindering dissipation of the membrane potential and perhaps helping to prevent ATP hydrolysis.

SUPPORTING INFORMATION AVAILABLE

Modeling using the steady state equations for NADH oxidation and equations for the two models of NAD^+ reduction. This material is available free of charge via the Internet at http://pubs.acs.org.

REFERENCES

1. Saraste, M. (1999) Oxidative phosphorylation at the fin de siècle, *Science 283*, 1488−1493.
2. Schultz, B. E., and Chan, S. I. (2001) Structures and proton-pumping strategies of mitochondrial respiratory enzymes, *Annu. Rev. Biophys. Biomol. Struct. 30*, 23−65.
3. Hirst, J., Carroll, J., Fearnley, I. M., Shannon, R. J., and Walker, J. E. (2003) The nuclear encoded subunits of complex I from bovine heart mitochondria, *Biochim. Biophys. Acta 1604*, 135−150.
4. Carroll, J., Fearnley, I. M., Skehel, J. M., Shannon, R. J., Hirst, J., and Walker, J. E. (2006) Bovine complex I is a complex of 45 different subunits, *J. Biol. Chem. 281*, 32724−32727.
5. Wikström, M. (1984) Two protons are pumped from the mitochondrial matrix per electron transferred between NADH and ubiquinone, *FEBS Lett. 169*, 300−304.
6. Brand, M. D., Affourtit, C., Esteves, T. C., Green, K., Lambert, A. J., Miwa, S., Pakay, J. L., and Parker, N. (2004) Mitochondrial superoxide: Production, biological effects, and activation of uncoupling proteins, *Free Radical Biol. Med. 37*, 755−767.
7. Smeitink, J., and van den Heuvel, L. (1999) Human mitochondrial complex I in health and disease, *Am. J. Hum. Genet. 64*, 1505−1510.
8. Orth, M., and Schapira, A. H. V. (2001) Mitochondria and degenerative disorders, *Am. J. Med. Genet. 106*, 27−36.
9. Wallace, D. C. (1999) Mitochondrial diseases in man and mouse, *Science 283*, 1482−1488.
10. Guénebaut, V., Schlitt, A., Weiss, H., Leonard, K., and Friedrich, T. (1998) Consistent structure between bacterial and mitochondrial NADH:ubiquinone oxidoreductase (complex I), *J. Mol. Biol. 276*, 105−112.
11. Ohnishi, T. (1998) Iron-sulfur clusters/semiquinones in complex I, *Biochim. Biophys. Acta 1364*, 186−206.
12. Sazanov, L. A., and Hinchliffe, P. (2006) Structure of the hydrophilic domain of respiratory complex I from *Thermus thermophilus*, *Science 311*, 1430−1436.
13. Ghisla, S., and Massey, V. (1989) Mechanisms of flavoprotein-catalyzed reactions, *Eur. J. Biochem. 181*, 1−17.
14. Moser, C. C., Farid, T. A., Chobot, S. E., and Dutton, P. L. (2006) Electron tunneling chains of mitochondria, *Biochim. Biophys. Acta 1757*, 1096−1109.
15. Mamedova, A. A., Holt, P. J., Carroll, J., and Sazanov, L. A. (2004) Substrate-induced conformational change in bacterial complex I, *J. Biol. Chem. 279*, 23830−23836.
16. Sled, V. D., and Vinogradov, A. D. (1993) Kinetics of the mitochondrial NADH-ubiquinone oxidoreductase interaction with hexammineruthenium (III), *Biochim. Biophys. Acta 1141*, 262−268.
17. Kussmaul, L., and Hirst, J. (2006) The mechanism of superoxide production by NADH:ubiquinone oxidoreductase (complex I) from bovine heart mitochondria, *Proc. Natl. Acad. Sci. U.S.A. 103*, 7607−7612.

18. Galante, Y. M., and Hatefi, Y. (1978) Resolution of complex I and isolation of NADH dehydrogenase and an iron-sulfur protein, *Methods Enzymol. 53*, 15−21.
19. Galante, Y. M., and Hatefi, Y. (1979) Purification and molecular and enzymic properties of mitochondrial NADH dehydrogenase, *Arch. Biochem. Biophys. 192*, 559−568.
20. Léger, C., Elliott, S. J., Hoke, K. R., Jeuken, L. J. C., Jones, A. K., and Armstrong, F. A. (2003) Enzyme electrokinetics: Using protein film voltammetry to investigate redox enzymes and their mechanisms, *Biochemistry 42*, 8653−8662.
21. Armstrong, F. A. (2005) Recent developments in dynamic electrochemical studies of adsorbed enzymes and their active sites, *Curr. Opin. Chem. Biol. 9*, 110−117.
22. Hirst, J. (2006) Elucidating the mechanisms of coupled electron transfer and catalytic reactions by protein film voltammetry, *Biochim. Biophys. Acta 1757*, 225−239.
23. Sazanov, L. A., Peak-Chew, S. Y., Fearnley, I. M., and Walker, J. E. (2000) Resolution of the membrane domain of bovine complex I into subcomplexes: Implications for the structural organization of the enzyme, *Biochemistry 39*, 7229−7235.
24. Hatefi, Y. (1978) Preparation and properties of NADH:ubiquinone oxidoreductase (complex I), *Methods Enzymol. 53*, 11−14.
25. Sled, V. D., and Vinogradov, A. D. (1993) Reductive inactivation of the mitochondrial three subunit NADH dehydrogenase, *Biochim. Biophys. Acta 1143*, 199−203.
26. Vuillard, L., Braun-Breton, C., and Rabilloud, T. (1995) Non-detergent sulfobetaines: A new class of mild solubilization agents for protein purification, *Biochem. J. 305*, 337−343.
27. Doeg, K. A., and Ziegler, D. M. (1962) Simplified methods for the estimation of iron in mitochondria and submitochondrial fractions, *Arch. Biochem. Biophys. 97*, 37−40.
28. Burch, H. B. (1957) Fluorimetric assay of FAD, FMN and riboflavin, *Methods Enzymol. 3*, 960−962.
29. Sharpley, M. S., Shannon, R. J., Draghi, F., and Hirst, J. (2006) Interactions between phospholipids and NADH:ubiquinone oxidoreductase (complex I) from bovine mitochondria, *Biochemistry 45*, 241−248.
30. Fearnley, I. M., Carroll, J., Shannon, R. J., Runswick, M. J., Walker, J. E., and Hirst, J. (2001) GRIM-19, a cell death regulatory gene product, is a subunit of bovine mitochondrial NADH: ubiquinone oxidoreductase (complex I), *J. Biol. Chem. 276*, 38345−38348.
31. Orr, G. A., and Blanchard, J. S. (1984) High-performance ion-exchange separation of oxidized and reduced nicotinamide adenine dinucleotides, *Anal. Biochem. 142*, 232−234.
32. Gavrikova, E. V., Grivennikova, V. G., Sled, V. D., Ohnishi, T., and Vinogradov, A. D. (1995) Kinetics of the mitochondrial three-subunit NADH dehydrogenase interaction with hexammineruthenium(III), *Biochim. Biophys. Acta 1230*, 23−30.
33. Ragan, C. I., Galante, Y. M., Hatefi, Y., and Ohnishi, T. (1982) Resolution of mitochondrial NADH dehydrogenase and isolation of two iron-sulfur proteins, *Biochemistry 21*, 590−594.
34. Ohnishi, T., Ragan, C. I., and Hatefi, Y. (1985) EPR studies of iron-sulfur clusters in isolated subunits and subfractions of NADH-ubiquinone oxidoreductase, *J. Biol. Chem. 260*, 2782−2788.
35. Zu, Y., di Bernardo, S., Yagi, T., and Hirst, J. (2002) Redox properties of the [2Fe-2S] center in the 24 kDa (NQO2) subunit of NADH:ubiquinone oxidoreductase (complex I), *Biochemistry 41*, 10056−10069.
36. Clark, W. M. (1960) *Oxidation-reduction potentials of organic systems*, The Williams and Wilkins Co., Baltimore.
37. Sled, V. D., Rudnitzky, N. I., Hatefi, Y., and Ohnishi, T. (1994) Thermodynamic analysis of flavin in mitochondrial NADH: ubiquinone oxidoreductase (complex I), *Biochemistry 33*, 10069−10075.
38. Heering, H. A., Weiner, J. H., and Armstrong, F. A. (1997) Direct detection and measurement of electron relays in a multicentered enzyme: Voltammetry of electrode-surface films of *E. coli* fumarate reductase, an iron-sulfur flavoprotein, *J. Am. Chem. Soc. 119*, 11628−11638.
39. Zu, Y., Shannon, R. J., and Hirst, J. (2003) Reversible, electrochemical interconversion of NADH and NAD$^+$ by the catalytic (Iλ) subcomplex of mitochondrial NADH:ubiquinone oxidoreductase (complex I), *J. Am. Chem. Soc. 125*, 6020−6021.
40. Mayhew, S. G. (1999) The effects of pH and semiquinone formation on the oxidation-reduction potentials of flavin mononucleotide, *Eur. J. Biochem. 265*, 698−702.
41. Léger, C., Jones, A. K., Albracht, S. P. J., and Armstrong, F. A. (2002) Effect of a dispersion of interfacial electron transfer rates on steady state catalytic electron transport in [NiFe]-hydrogenase and other enzymes, *J. Phys. Chem. B 106*, 13058−13063.
42. Hoke, K. R., Cobb, N., Armstrong, F. A., and Hille, R. (2004) Electrochemical studies of arsenite oxidase: An unusual example of a highly cooperative two-electron molybdenum center, *Biochemistry 43*, 1667−1674.
43. Reda, T., and Hirst, J. (2006) Interpreting the catalytic voltammetry of an adsorbed enzyme by considering substrate mass transfer, enzyme turnover, and interfacial electron transport, *J. Phys. Chem. B 110*, 1394−1404.
44. Heering, H. A., Hirst, J., and Armstrong, F. A. (1998) Interpreting the catalytic voltammetry of electroactive enzymes adsorbed on electrodes, *J. Phys. Chem. B 102*, 6889−6902.
45. Vinogradov, A. D. (1993) Kinetics, control and mechanism of ubiquinone reduction by the mammalian respiratory chain-linked NADH:ubiquinone reductase, *J. Bioenerg. Biomembr. 25*, 367−375.
46. Avraam, R., and Kotlyar, A. B. (1992) Kinetics of NADH oxidation and NAD$^+$ reduction by mitochondrial complex I, *Biochemistry (Moscow) 56*, 1181−1189.
47. Léger, C., Heffron, K., Pershad, H. R., Maklashina, E., Luna-Chavez, C., Cecchini, G., Ackrell, B. A. C., and Armstrong, F. A. (2001) Enzyme electrokinetics: Energetics of succinate oxidation by fumarate reductase and succinate dehydrogenase, *Biochemistry 40*, 11234−11245.
48. Elliott, S. J., McElhaney, A. E., Feng, C., Enemark, J. H., and Armstrong, F. A. (2002) A voltammetric study of interdomain electron transfer within sulfite oxidase, *J. Am. Chem. Soc. 124*, 11612−11613.
49. Heering, H. A., Wiertz, F. G. M., Dekker, C., and de Vries, S. (2004) Direct immobilization of native yeast iso-1 cytochrome c on bare gold: Fast electron relay to redox enzymes and zeptomole protein-film voltammetry, *J. Am. Chem. Soc. 126*, 11103−11112.
50. Haas, A. S., Pilloud, D. L., Reddy, K. S., Babcock, G. T., Moser, C. C., Blasie, J. K., and Dutton, P. L. (2001) Cytochrome c and cytochrome c oxidase: Monolayer assemblies and catalysis, *J. Phys. Chem. B 105*, 11351−11362.
51. Hirst, J., Sucheta, A., Ackrell, B. A. C., and Armstrong, F. A. (1996) Electrocatalytic voltammetry of succinate dehydrogenase: Direct quantification of the catalytic properties of a complex electron-transport enzyme, *J. Am. Chem. Soc. 118*, 5031−5038.
52. Léger, C., Lederer, F., Guigliarelli, B., and Bertrand, P. (2006) Electron flow in multicenter enzymes: Theory, applications, and consequences on the natural design of redox chains, *J. Am. Chem. Soc. 128*, 180−187.
53. Hille, R., and Anderson, R. F. (2001) Coupled electron/proton transfer in complex flavoproteins, *J. Biol. Chem. 276*, 31193−31201.
54. Elliott, S. J., Léger, C., Pershad, H. R., Hirst, J., Heffron, K., Ginet, N., Blasco, F., Rothery, R. A., Weiner, J. H., and Armstrong, F. A. (2002) Detection and interpretation of redox potential optima in the catalytic activity of enzymes, *Biochim. Biophys. Acta 1555*, 54−59.
55. Sucheta, A., Ackrell, B. A. C., Cochran, B., and Armstrong, F. A. (1992) Diode-like behavior of a mitochondrial electron-transport enzyme, *Nature 356*, 361−362.
56. Gatti, D. L., Palfey, B. A., Lah, M. S., Entsch, B., Massey, V., Ballou, D. P., and Ludwig, M. L. (1994) The mobile flavin of 4-OH benzoate hydroxylase, *Science 266*, 110−114.
57. Angove, H. C., Cole, J. A., Richardson, D. J., and Butt, J. N. (2002) Protein film voltammetry reveals distinctive fingerprints of nitrite and hydroxylamine reduction by a cytochrome c nitrite reductase, *J. Biol. Chem. 277*, 23374−23381.
58. Gwyer, J. D., Richardson, D. J., and Butt, J. N. (2004) Resolving complexity in the interactions of redox enzymes and their inhibitors: Contrasting mechanisms for the inhibition of a cytochrome c nitrite reductase revealed by protein film voltammetry, *Biochemistry 43*, 15086−15094.
59. Gwyer, J. D., Richardson, D. J., and Butt, J. N. (2005) Diode or tunnel diode characteristics? Resolving the catalytic consequences

of proton coupled electron transfer in a multi-centered oxidoreductase, *J. Am. Chem. Soc. 127*, 14964−14965.

60. Hudson, J. M., Heffron, K., Kotlyar, V., Sher, Y., Maklashina, E., Cecchini, G., and Armstrong, F. A. (2005) Electron transfer and catalytic control by the iron-sulfur clusters in a respiratory enzyme, *E. coli* fumarate reductase, *J. Am. Chem. Soc. 127*, 6977−6989.
61. Heffron, K., Léger, C., Rothery, R. A., Weiner, J. H., and Armstrong, F. A. (2001) Determination of an optimal potential window for catalysis by *E. coli* dimethyl sulfoxide reductase and hypothesis on the role of Mo(V) in the reaction pathway, *Biochemistry 40*, 3117−3126.
62. Elliott, S. J., Hoke, K. R., Heffron, K., Palak, M., Rothery, R. A., Weiner, J. H., and Armstrong, F. A. (2004) Voltammetric studies of the catalytic mechanism of the respiratory nitrate reductase from *E. coli*: How nitrate reduction and inhibition depend on the oxidation state of the active site, *Biochemistry 43*, 799−807.
63. Anderson, L. J., Richardson, D. J., and Butt, J. N. (2001) Catalytic protein film voltammetry from a respiratory nitrate reductase provides evidence for complex electrochemical modulation of enzyme activity, *Biochemistry 40*, 11294−11307.
64. Frangioni, B., Arnoux, P., Sabaty, M., Pignol, D., Bertrand, P., Guigliarelli, B., and Léger, C. (2004) In *Rhodobacter sphaeroides* respiratory nitrate reductase, the kinetics of substrate binding favors intramolecular electron transfer, *J. Am. Chem. Soc. 126*, 1328−1329.
65. Jepson, B. J. N., Anderson, L. J., Rubio, L. M., Taylor, C. J., Butler, C. S., Flores, E., Herrero, A., Butt, J. N., and Richardson, D. J. (2004) Tuning a nitrate reductase for function, *J. Biol. Chem. 279*, 32212−32218.
66. Chance, B., Lees, H., and Postgate, J. R. (1972) The meaning of 'reversed electron flow' and 'high energy electron' in biochemistry, *Nature 238*, 330−331.

BI061988Y